2009

# Microseismicity at the North Anatolian Fault in the Sea of Marmara offshore Istanbul, NW Turkey

Fatih Bulut
*GFZ German Research Center for Geosciences*

Marco Bohnhoff
*GFZ German Research Center for Geosciences*

William L. Ellsworth
*U.S. Geological Survey*

Mustafa Aktar
*Kandilli Observatory and Earthquake Research Institute*

Georg Dresen
*GFZ German Research Center for Geosciences*

JOURNAL OF GEOPHYSICAL RESEARCH, VOL. 114, B09302, doi:10.1029/2008JB006244, 2009

# Microseismicity at the North Anatolian Fault in the Sea of Marmara offshore Istanbul, NW Turkey

Fatih Bulut,[1] Marco Bohnhoff,[1] William L. Ellsworth,[2] Mustafa Aktar,[3] and Georg Dresen[1]

Received 9 December 2008; revised 28 April 2009; accepted 8 June 2009; published 3 September 2009.

[1] The North Anatolian Fault Zone (NAFZ) below the Sea of Marmara forms a "seismic gap" where a major earthquake is expected to occur in the near future. This segment of the fault lies between the 1912 Ganos and 1999 İzmit ruptures and is the only NAFZ segment that has not ruptured since 1766. To monitor the microseismic activity at the main fault branch offshore of Istanbul below the Çınarcık Basin, a permanent seismic array (PIRES) was installed on the two outermost Prince Islands, Yassiada and Sivriada, at a few kilometers distance to the fault. In addition, a temporary network of ocean bottom seismometers was deployed throughout the Çınarcık Basin. Slowness vectors are determined combining waveform cross correlation and P wave polarization. We jointly invert azimuth and traveltime observations for hypocenter determination and apply a bootstrap resampling technique to quantify the location precision. We observe seismicity rates of 20 events per month for $M < 2.5$ along the basin. The spatial distribution of hypocenters suggests that the two major fault branches bounding the depocenter below the Çınarcık Basin merge to one single master fault below ~17 km depth. On the basis of a cross-correlation technique we group closely spaced earthquakes and determine composite focal mechanisms implementing recordings of surrounding permanent land stations. Fault plane solutions have a predominant right-lateral strike-slip mechanism, indicating that normal faulting along this part of the NAFZ plays a minor role. Toward the west we observe increasing components of thrust faulting. This supports the model of NW trending, dextral strike-slip motion along the northern and main branch of the NAFZ below the eastern Sea of Marmara.

**Citation:** Bulut, F., M. Bohnhoff, W. L. Ellsworth, M. Aktar, and G. Dresen (2009), Microseismicity at the North Anatolian Fault in the Sea of Marmara offshore Istanbul, NW Turkey, *J. Geophys. Res.*, *114*, B09302, doi:10.1029/2008JB006244.

## 1. Introduction

[2] The North Anatolian Fault Zone (NAFZ) represents one of the largest plate-bounding transform faults separating the Anatolia and Eurasian plates and extending for ~1600 km between Eastern Anatolian and the Northern Aegean. Westward movement of Anatolia has developed in the framework of the northward moving Arabian plate and the Hellenic subduction zone where the African lithosphere is subducted below the Aegean. Current right-lateral slip rate along the fault is 20–30 mm/a [e.g., *Barka*, 1992, *McClusky et al.*, 2000] repeatedly producing major strike-slip earthquakes but also N-S extensional normal faulting events south of the Marmara region. During the 20th century, the NAFZ has ruptured over 900 km of its length [*Ambraseys*, 1970; *Barka*, 1999]. A series of large earthquakes starting in 1939 near Erzincan in eastern Anatolia propagated westward toward the Istanbul-Marmara region in northwestern Turkey where the 1999 İzmit earthquake occurred (Figure 1a). West of the İzmit rupture a "seismic gap" spans along a >100 km long segment below the Sea of Marmara [e.g., *Töksöz et al.*, 1979; *Stein et al.*, 1997; *Reilinger et al.*, 2000] (see Figure 1a). The Marmara segment connects the 1912 Ganos and 1999 İzmit ruptures and has not ruptured since 1766. Assuming current slip rates it may have accumulated a slip deficit of up to 4–5 m. It is believed being capable of generating a $M \geq 7.4$ earthquake [*Hubert-Ferrari et al.*, 2000] or a number of smaller normal faulting events [*Armijo et al.*, 2002]. However, it could even rupture in a large single event [*Le Pichon et al.*, 1999]. Dynamic modeling of earthquakes for the Marmara segment on that zone indicates that the nucleation location has a significant effect on size, rupture propagation and final slip of an upcoming event [*Oglesby et al.*, 2008].

[3] The two most recent major earthquakes in NW Turkey occurred in 1999 (Mw7.4 İzmit and Mw7.1 Düzce events, Figure 1a) rupturing a ~200 km long segment of NAFZ east of the Marmara region [e.g., *Tibi et al.*, 2001; *Barka et al.*, 2002; *Aktar et al.*, 2004]. Both main shocks

[1]Helmholtz Centre Potsdam, GFZ German Research Centre for Geosciences, Section 3.2, Geomechanics and Rheology, Potsdam, Germany.
[2]U.S. Geological Survey, Menlo Park, California, USA.
[3]Kandilli Observatory and Earthquake Research Institute, Boğaziçi University, Istanbul, Turkey.


0148-0227/09/2008JB006244$09.00

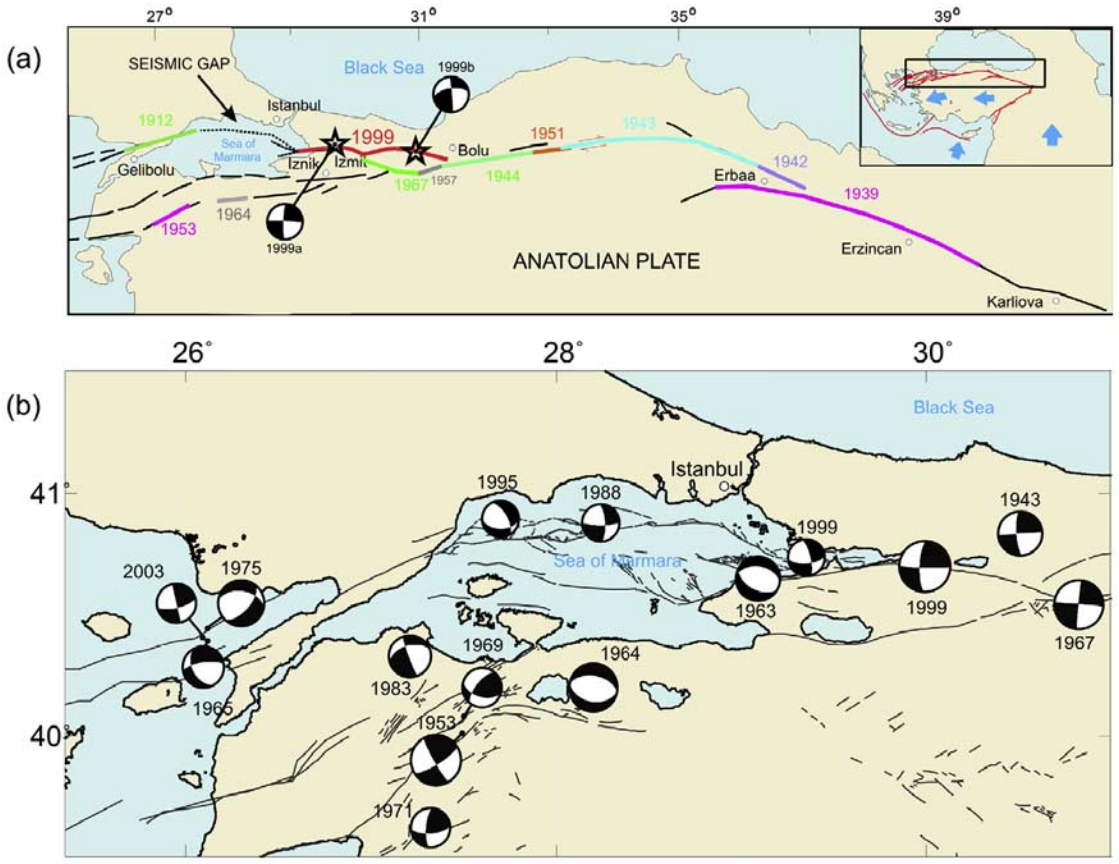


**Figure 1.** (a) Tectonic map of Anatolian-Aegean region (modified from *U.S. Geological Survey* [2000]): Westward movement of Anatolian plate causes destructive earthquakes along North Anatolian Fault Zone (black line). Rupture zones associated with destructive earthquakes are represented by different colors. In this study we focused on the westernmost part of 1999 (İzmit 17 August 1999 Mw 7.4 and Düzce 12 November 1999 Mw 7.2) rupture zone in which a destructive earthquake is expected to occur in the next decades. (b) Fault plane solution for M > 5.0 size earthquakes occurred within the vicinity of Sea of Marmara region since 1943 (compiled from *Örgülü and Aktar,* [2001], *Pinar et al.* [2003], and *Şengör et al.* [2005]). Fault lines taken from Turkey General Directorate of Mineral Research and Exploration, and *Armijo et al.* [2005].

had a (pure) dextral strike-slip mechanism reflecting the overall characteristic of the NAFZ. In the case of the İzmit event the rupture extended from the eastern Sea of Marmara to the Düzce area. There, the subsequent Düzce event occurred 87 days later extending the rupture by another 50 km to the East (see Figure 1a). The western end of the 1999 rupture is located in the eastern Sea of Marmara below the Çınarcık Basin (CB) [e.g., *Wright et al.*, 2001]. The rupture may have extended to just south of the Princes Islands [*Bouchon et al.*, 2002; *Özalaybey et al.*, 2002] that are located within ~20 km distance to the city of Istanbul with its >12.5 million inhabitants. In contrast, *Pinar et al.* [2001] argue that the rupture did not enter the Çınarcık Basin but terminated close to Hersek, west of the İzmit Gulf. The İzmit event ruptured in distinct segments and the same segmentation was observed from analysis of aftershock focal mechanisms [*Bohnhoff et al.*, 2006]. At the western end of the İzmit rupture a branching of the NAFZ is observed with streaks of similar normal or strike-slip faulting mechanisms along individual fault branches below the Çınarcık Basin [*Örgülü and Aktar*, 2001; *Özalaybey et al.*, 2002; *Karabulut et al.*, 2002]. The estimated 30-year probability for an event M ≥ 7 below the Sea of Marmara is 35–70% [e.g., *Wright et al.*, 2001; *Parsons et al.*, 2000; *Parsons*, 2004].

[4] In this study, we present results of a microseismic monitoring campaign conducted throughout the Çınarcık Basin and on the Prince Islands at the northern escarpment of the Çınarcık Basin. Our objective is to determine the seismotectonic setting along the eastern part of the Marmara "seismic gap" based on microseismic recordings with unprecedented low magnitude detection threshold. Results are related to existing structural information available for the area and discussed in the light of an expected major earthquake at this segment of the NAFZ.

## 2. PIRES: A Seismic Array on the Prince Islands

[5] Earthquake hypocenters in the Marmara region obtained by the regional seismic network operated by Kandilli Observatory and Earthquake Research Institute (KOERI hereafter) broadly define the major branches of

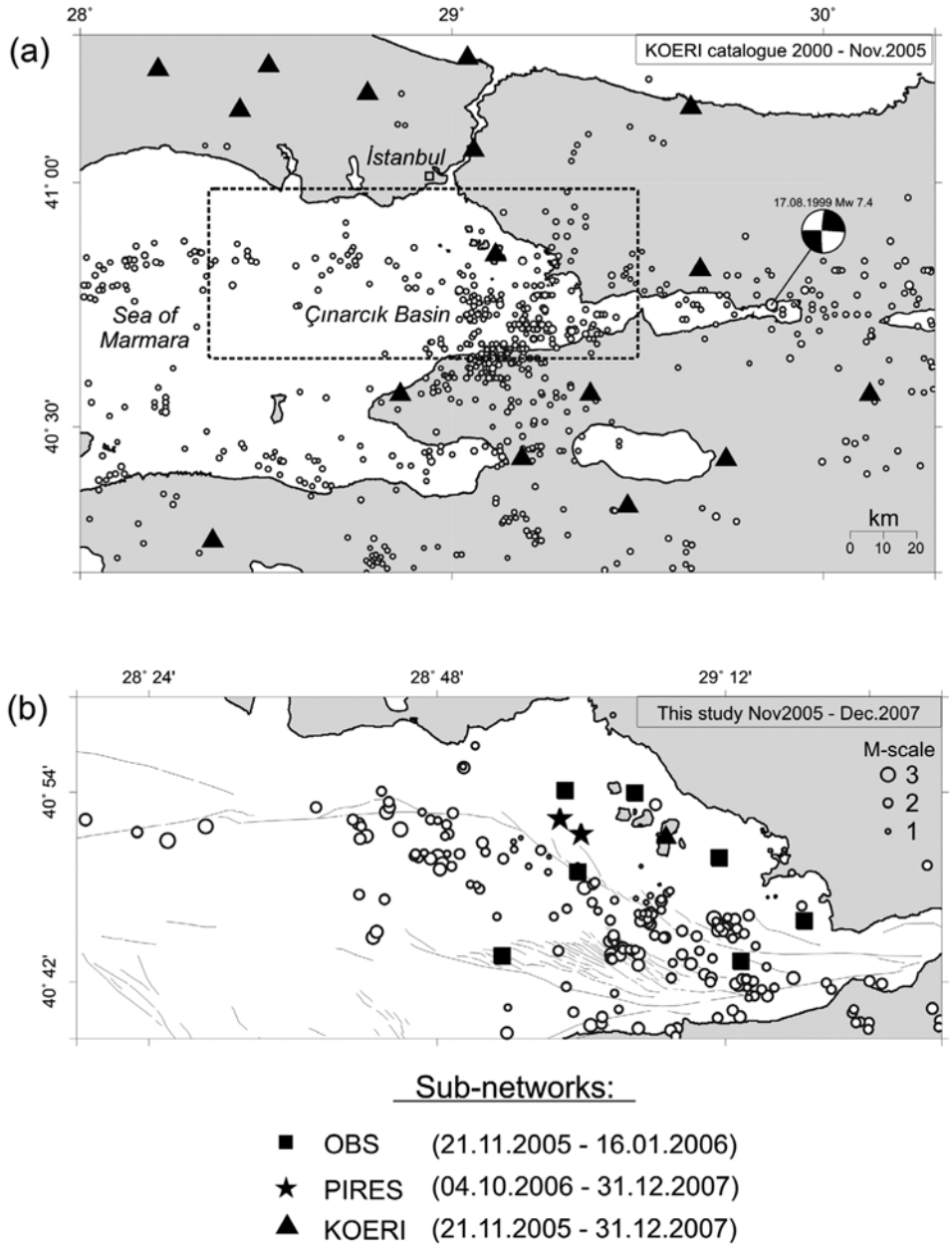


**Figure 2.** (a) Seismic activity in eastern Marmara region based on KOERI catalog for the time period January 2000 to November 2005. (b) Seismic activity in Çınarcık Basin after the analysis of combined data from OBS (squares), PIRES (stars), and KOERI seismic networks for the time period of November 2005 to December 2007. Segmentation of NAFZ in the Sea of Marmara (gray lines) is obtained from *Armijo et al.* [2005].

the NAFZ in NW Turkey (see Figure 2a). However, the main branches of the NAFZ are located offshore in the Sea of Marmara where there are no near stations, resulting in a catalog magnitude of completeness (Mc) of Mc $\sim$ 2.6. Hypocenter precision is also limited by the station geometry, making it difficult to relate seismicity to individual fault structures.

[6] In order to improve the detection threshold and hypocenter accuracy for microseismicity below the Çınarcık Basin we first deployed a temporary network of eight ocean bottom seismometers extending throughout the Çınarcık Basin between November 2005 and January 2006 (Figure 2b). The position of each OBS on the seafloor was determined using two-way traveltimes of acoustic signals sent from the boat to the OBS while circumnavigating the instrument. The clock drift was linearly interpolated from the measured drift after recovery of the instrument. Timing systems of two of the OBS stations were out of order. From these stations only the S-P times were used. We obtained an average station azimuthal gap of 137° combining the OBSs with the KOERI land stations. Combined network allowed us to locate 17 well-constrained microearthquakes along the basin during the 55-day period of OBS campaign ($M < 2.5$, err $< 5.0$ km, RMS $< 0.3$). This observation confirmed that currently a

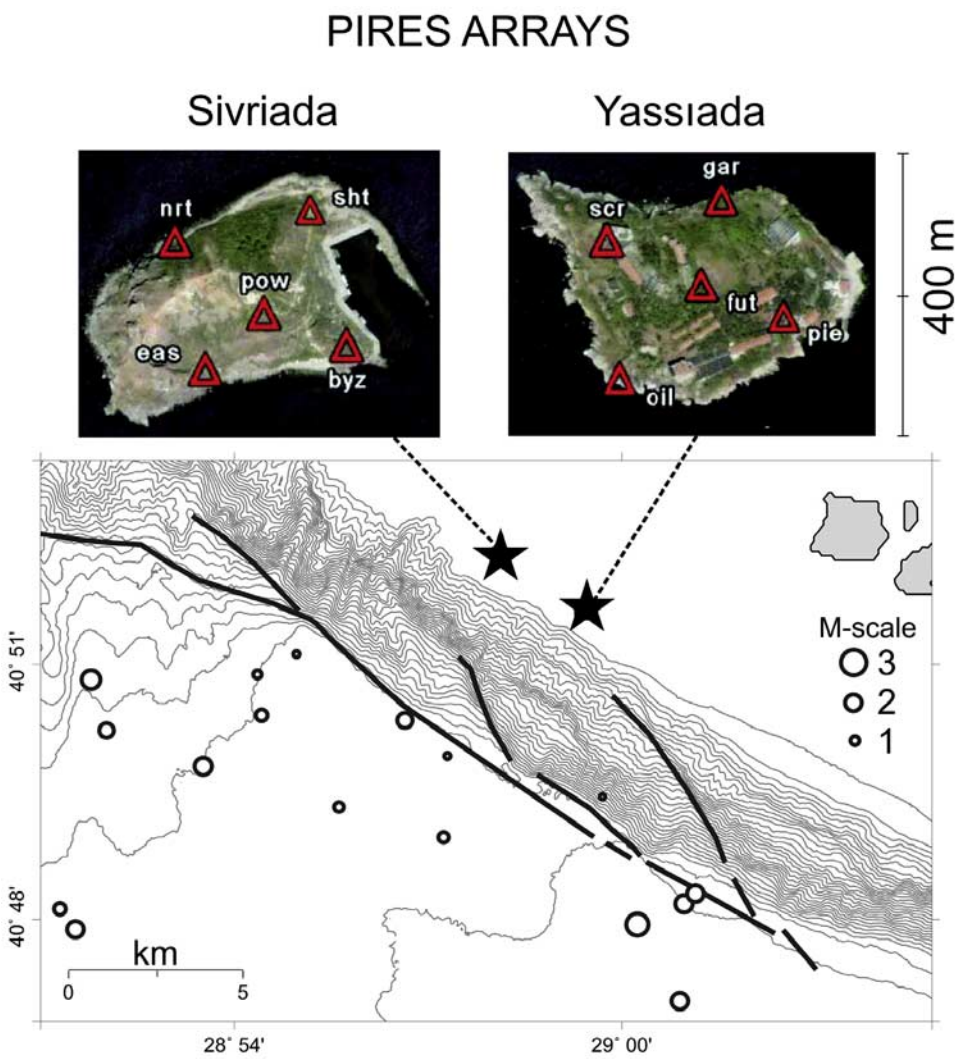


**Figure 3.** Configuration of PIRES subarrays on two outer Princes Islands (left) Yassıada and (right) Sivriada located at ∼5 km distance to the northern slope of Çınarcık Basin. Seismic stations are indicated by red triangles. Circles indicate the well-located hypocenters detected by PIRES arrays.

significant amount of microseicmic activity occurs along the Çınarcık Basin segments of NAFZ.

[7] In a second step designed to improve long-term monitoring we installed a seismic array (Prince Islands Real-time Earthquake System, PIRES) on the two outermost Prince Islands, Sivriada and Yassiada. PIRES consists of two subarrays of five stations on each island and is located less than 5 km to the north of the surface trace of the main fault branch (Figure 3). Both subarrays include a cross-shaped distribution of stations with an aperture of ∼300 m. The average station spacing within each PIRES subarray is 191 m. Establishing the PIRES network was a major logistic task since none of the islands are inhabited or connected by regular ferry traffic. To allow secure long-term operation and to protect stations from unauthorized access, concrete housings were constructed. Stations are operated autonomously and run on solar panels. PIRES went into operation in autumn 2006 with nine short-period stations equipped with MARK L4−3C seismometers of 1 Hz natural frequency and one broadband sensor of type STS2. All stations are equipped with three component sensors. Data are sampled at 200 Hz. In this study, we analyze recordings covering the time period 4 October 2006 to 31 December 2007. Events were detected using a STA/LTA (short-term average/long-term average) trigger. Event windows are extracted once the signal-to-noise ratio (SNR) simultaneously exceeds a given threshold at a minimum of six stations. For a better coverage of local events the database includes additional data recorded at selected land stations of the regional seismic network (operated by KOERI).

[8] The data is recovered by periodic exchange of hard disk storage every three months. A waveform example obtained by PIRES station is shown in Figure 4a (local event at 7.1 km epicentral distance). During the recording period considered in this study we analyzed a total of 416 detected events that were evaluated using the procedure as discussed in the following.

## 3. Array Processing

[9] Many of the events detected by the PIRES array were not observed on the regional seismic network. As a conse-

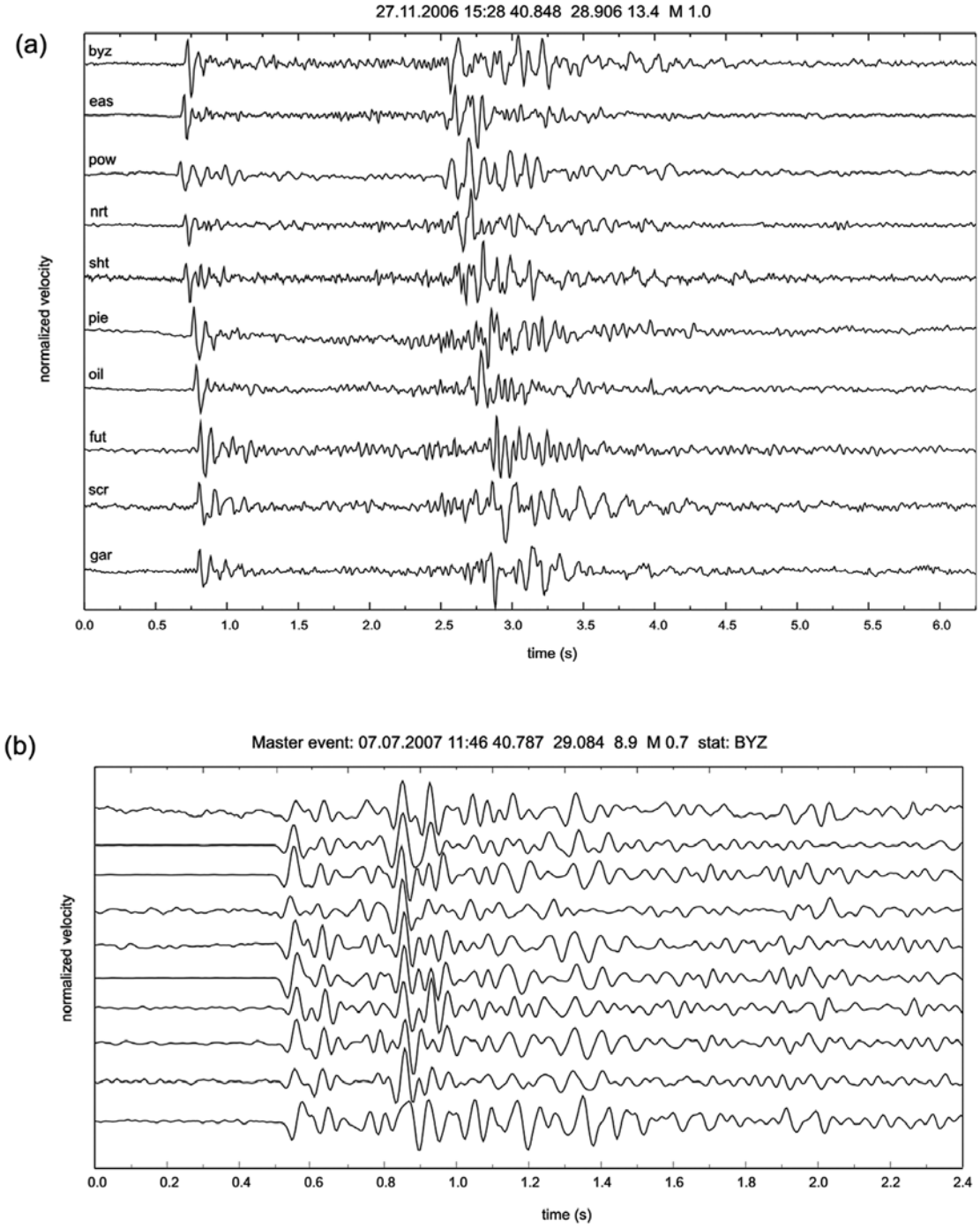


**Figure 4.** (a) Normalized velocity seismograms recorded by PIRES arrays. Initial cycles of P wave train are correlated to measure relative arrival times and then inverted to estimate the direction of incoming waves. Minor offshore events cannot be recorded by land stations and therefore we combine hand-picked P and S wave arrivals with azimuth estimates to better constrain the hypocenters. (b) P wave train of closely located earthquakes at station BYZ. We perform composite fault plane solutions combining the first motion data of events with similar waveforms.

quence, we use a combination of array-based methods to determine the azimuth and slowness of the body waves and traveltime measurements to determine the event hypocenters. We estimate the direction of incoming waves integrating (section 3.1) cross-correlation–derived azimuth and (section 3.2) incidence angle derived from polarization analysis. An initial guess for hypocenter location is forwardly defined by 1-D ray tracing fitting the S-P times. We (section 3.3) jointly invert arrival times and azimuth observations to determine the correction vectors from the initial guess to the final hypocenter (section 3.4). Uncertainty of the final locations is estimated using bootstrap resampling technique.

### 3.1. Azimuth

[10] P wave delays observed within an array of seismic sensors can be used to estimate the direction of incoming P wave. Because the PIRES network aperture is small compared to source-receiver distance, coherent waveforms observed across the array can be approximated as plane waves. Manually picked arrival times, however, are typically uncertain by 0.1 s (20 samples) and do not provide sufficient precision due to the very small aperture size of the PIRES subarrays. On the other hand, arrival times measured by waveform cross correlation can achieve differential arrival time accuracy of several milliseconds or better [*Poupinet et al.*, 1984]. Previous studies show that this technique can also be successfully used to obtain accurate estimates of P wave directions propagating across an array [*Frankel et al.*, 1991; *Cansi et al.*, 1993]. Here, we perform cross correlation in the time domain for the first four wavelengths after the P onset. We check the alignment of the correlated waveforms to minimize the cycle skip problem. Figure 4b illustrates a correlation windows defined for a characteristic event (vertical components for a M = 2.4 event at 24.4 km distance).

[11] The differential arrival time of a plane wave *dt* between two stations in the array can be expressed in terms of the differential location of the station pair ($r_x$, $r_y$, $r_z$) and the slowness vector ($u_x$, $u_y$, $u_z$) of the wave:

$$dt = r_x u_x + r_y u_y + r_z u_z. \tag{1}$$

Combining equation (1) from all possible station pairs for an event to a system of linear equations, the forward problem becomes

$$\mathbf{Gm} = \mathbf{d}, \tag{2}$$

where **G** defines a design matrix containing relative positions of station pairs, **m** represents the unknown slowness, and **d** is the data vector containing the observed P wave delays. We invert the **G** matrix to estimate the azimuth of P wave using the ratio between the horizontal components of the slowness **U**. The slowness error is estimated using the model covariance matrix $\mathbf{C} = \mathbf{V}\mathbf{A}^{-2}\mathbf{V}^{\mathbf{T}}$ based on singular value decomposition $\mathbf{G} = \mathbf{U}\mathbf{A}\mathbf{V}^{\mathbf{T}}$, where **A** is a diagonal matrix of the singular values, **U** and **V** are singular vectors [*Menke*, 1984; *Bokelmann*, 1995]. Data outliers (i.e., GPS timing errors, cycle skipping) are identified and eliminated using a cross-validation technique [*Segall and Matthews*, 1988].

[12] In order to quantify the sensitivity of the cross-correlation technique for azimuth observation at the PIRES array we compare cross-correlation–derived azimuths with the theoretical ones calculated for well-constrained hypocenters in Marmara region (Figure 5a). The hypocenters were determined by combining traveltime data from the KOERI network with arrival times measured on the PIRES array. A total of 192 events out of the total of 416 local detections were matched following this procedure. Azimuth observations converge to the theoretical azimuths with a mean misfit angle of 12°.

[13] Azimuth derived from cross correlation compare favorably to the theoretical azimuths. Error bars typically overlap suggesting that the covariance-based error estimates for cross-correlation–derived azimuth observations are reliable. The distribution of azimuth residuals is investigated with respect to different azimuths and event distances (Figure 5b). Error estimates are substantially higher than the absolute azimuth residuals for certain angular ranges, especially at azimuths between 240° and 300°. The results exemplify the precision and robustness for all observed ranges of azimuth and event distances. Average correlation coefficients as well as numbers of station pairs are compared to the absolute azimuth residuals (Figures 5c and 5d). The most prominent factor affecting the quality of the resulting azimuth is the number of station pairs used for azimuth determination. Figure 5c shows that precise azimuth estimations are expected for >10 station pairs.

### 3.2. Incidence Angle

[14] All PIRES stations are equipped with three-component sensors and allow stable estimates of the slowness by averaging P wave polarizations observed from the individual sensors. We estimate the incidence angle separately using polarization analysis as described by *Jurkevics* [1988]. The polarization ellipse is computed within moving time windows by solving the eigenproblem for the covariance matrix. **X** represents the three-component (*Z*, *E*, and *N*) zero mean displacement data in a time window. The covariance matrix is then computed as:

$$S = \frac{\mathbf{X}\mathbf{X}^T}{N}, \tag{3}$$

where *N* is the number of samples. The principal axes of the polarization ellipsoid are found by solving the eigenproblem for the covariance matrix *S*. Eigenvalues ($\lambda_1$, $\lambda_2$, $\lambda_3$) and eigenvectors ($\mathbf{u}_1$, $\mathbf{u}_2$, $\mathbf{u}_3$) give three principal axes of ellipsoid by $\lambda_j \mathbf{u}_j$ ($j$ = 1,.,3), where the eigenvectors are axis orientations and eigenvalues are their amplitudes. For each sensor, the incidence angle is given by

$$\text{Incidence} = \cos^{-1} |\mathbf{u}_{11}|. \tag{4}$$

We assume that the incidence angle of the incoming P wave can be represented by the direction of the largest linear polarization associated with the largest eigenvalue as the degree of rectilinearity is above 0.8. We represent the incidence angle at the array by averaging the polarization-based observations form the individual sensors. Reliability of the incidence is quantified by the standard deviation of the observations.

### 3.3. Joint Inversion for Hypocentral Parameters

[15] In those cases when an event was not detected at the mainland stations we jointly invert both azimuth and traveltime observations from the PIRES array to determine the hypocenter. Joint inversion of arrival time and direction of P wavefield was applied earlier [*Lienert and Havskov*, 1995; *Oye and Roth*, 2003] and improved the results significantly in case of large azimuthal gaps of instrumentation. Here we adopt the approach applied by *Lienert and Havskov* [1995]. Input consists of P and S wave arrival tunes, S-P times and the direction of P wave. A trial hypocenter is defined by the slowness of the incoming P

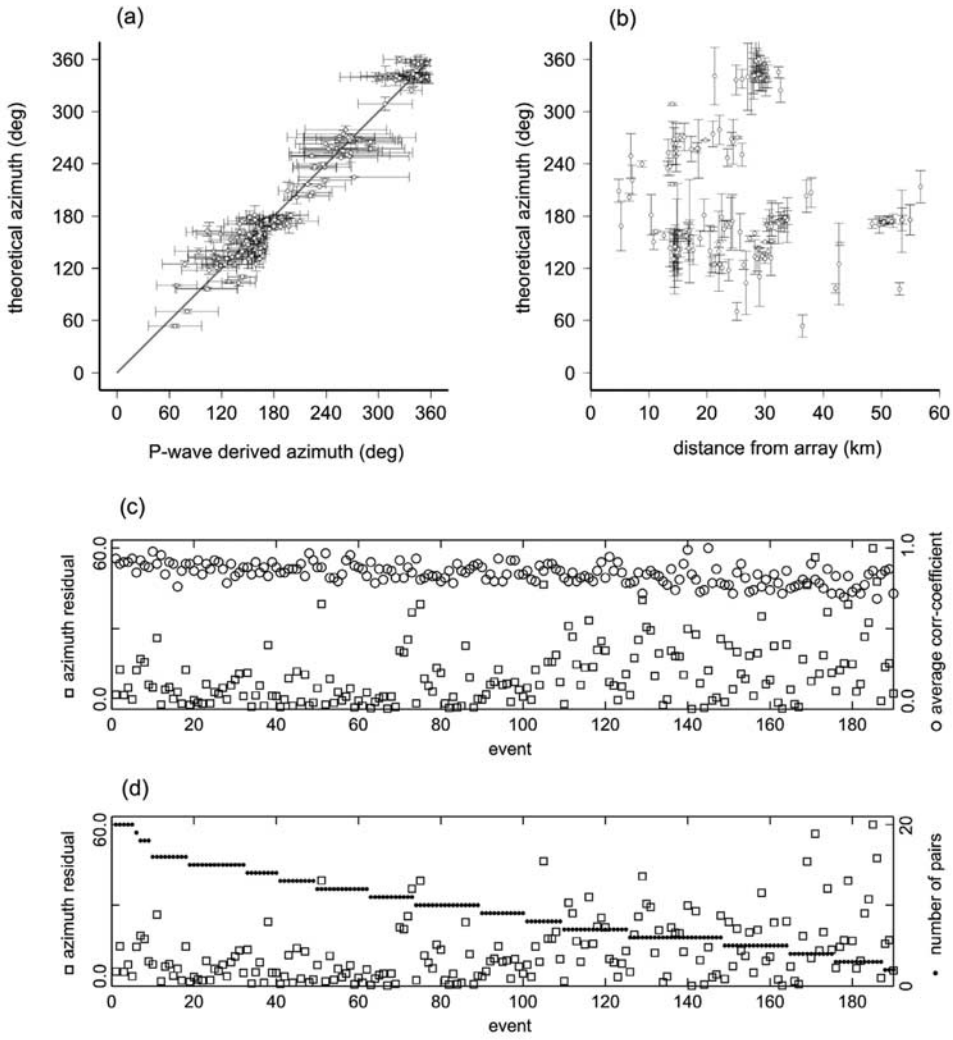


**Figure 5.** (a) Cross-correlation–derived azimuth observations are compared to the theoretical azimuth calculated for well-determined hypocenters. Error bars for azimuth observations represent the error estimates obtained from covariance matrix, and for theoretical calculated from the uncertainty of absolute locations. (b) Distribution of azimuth residuals (error bars) with respect to theoretical azimuth and event distance from the PIRES array. Azimuth residuals are compared with (c) average cross-correlation coefficient and (d) number of data to see the basic factor affecting the quality of azimuth observations.

wave and S-P time using 1-D ray tracing. We note that the convergence to the true model parameters strongly depends on the accuracy of the velocity model. In a second step, arrival times and azimuth observations are incorporated in the Geiger's linearized inversion. Partial derivatives of both azimuth observations ($Az$ in equation (6)) and arrival times ($T$ in equation (5)) are included in the inversion.

$$r_i = \frac{\partial T}{\partial x_i}\Delta x + \frac{\partial T}{\partial y_i}\Delta y + \frac{\partial T}{\partial z_i}\Delta z + \Delta t \tag{5}$$

$$r_i^{Az} = \frac{\partial Az}{\partial x_i}\Delta x + \frac{\partial Az}{\partial y_i}\Delta y \tag{6}$$

The assumption is that the residuals ($r_i$, $r_i^{Az}$) are due to the error in the initial guess of hypocenters and must be minimized by the correction vectors of initial guess $\Delta x$, $\Delta y$, $\Delta z$, $\Delta t$. Beside the individual weightings, event distance is considered to normalize the weighting of azimuth to arrival time data. The system of linear equations has to be solved iteratively as designed with respect to the difference of model parameters. Inversion starts from a trial location and its computed data residual vector. The trial location and, therefore, data vector are updated for subsequent iterations according to the damped model parameters. The iterative procedure is stopped once the smallest misfit is obtained and final hypocenter is defined.

### 3.4. Uncertainty Estimation

[16] Uncertainty of the hypocenter is commonly estimated by the variance of model parameters obtained for the best fit [e.g., *Lienert and Havskov*, 1995]. Here, we use an alternative approach to estimate confidence intervals of the final locations based on the bootstrap procedure [*Efron*,

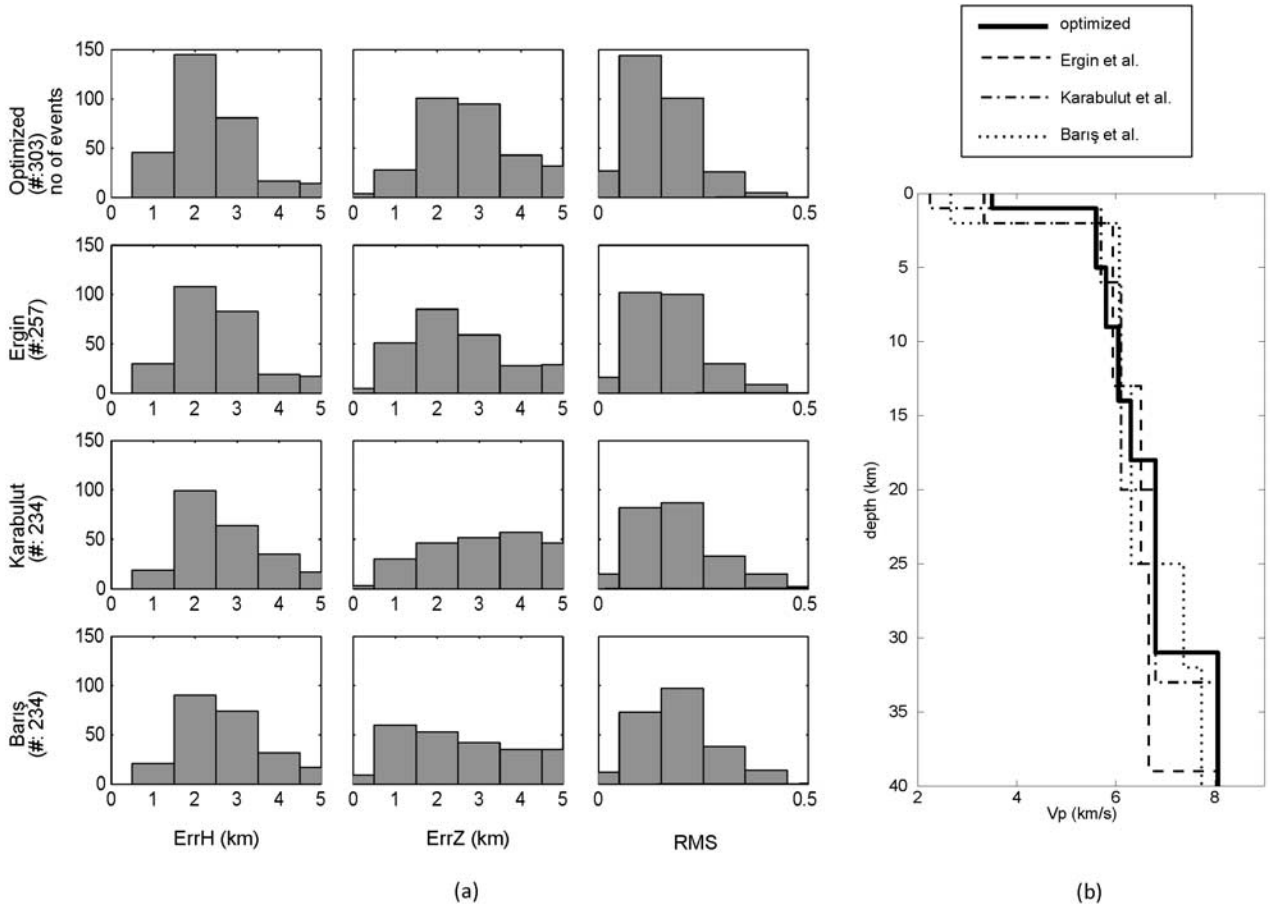


**Figure 6.** (a) Comparison of the hypocenter specifications of inversion-derived velocity model with the results based on the other models. (b) Dashed lines represent the 1-D models proposed earlier for the region, and solid line is the model optimized for the crustal coverage of our combined network (P wave velocity (km/s) of [3.50 5.60 5.80 6.05 6.30 6.80 8.05], depths (km) of [0.0 0.5 5.0 9.0 14.0 18.00 30.0]).

1982]. The bootstrap method was previously applied for estimating uncertainty of relative hypocenters [*Shearer*, 1997; *Waldhauser and Ellsworth*, 2000] and absolute hypocenters determined using array data [*Oye and Roth*, 2003]. After determining a final hypocenter for a particular event, we draw a random sample, with replacement, from the final residual distribution and solve for a new hypocenter. The procedure is repeated 250 times for which statistical properties of the results are stable. The uncertainty of the final location is derived from the distribution of reproduced bootstrap results about the final hypocenter.

## 4. Hypocenter Catalog and Local Velocity Model

[17] The importance of finding an appropriate local velocity model to locate microseismicity is well known [*Kissling et al.*, 1994]. The best available velocity model for the Çınarcık Basin is a regional 1-D model that does not consider the strong lateral variations across the basin down to ~5 km depth. However, most of the events recorded by PIRES have hypocentral distances of >10 km and occur at >5 km depth and are probably not affected by shallow lateral velocity variations. We used the VELEST simultaneous inversion code [*Kissling et al.*, 1994] to optimize the local 1-D velocity model. We carefully filter the event database to keep the inversion process from large instabilities that can be introduced by hypocenters with substantial uncertainties. As we aim at reducing uncertainties in location related to the velocity model, we only used high-quality events for which the location error is <3.0 km in both lateral and vertical direction, that have an RMS value smaller than 0.3 s, and that were recorded at least six mainland stations. We first defined the first-order layering of the crust by a trial-and-error approach minimizing normalized distribution of both RMS and the location errors. We repeat the process for large number of thin layers (2 km) and then combined layers with similar velocity values. The final inversion was performed using 179 events with 2104 P and 1545 S arrival times. S wave readings were used to better constrain the earthquake locations assuming a fixed ratio of P and S wave velocities, $V_p/V_s$ = 1.73. Using the improved model for hypocenter location resulted in significantly reduced traveltime residuals. This was also confirmed by comparing the new optimized model to others velocity models proposed earlier for the eastern Sea of Marmara region (Figure 6).

[18] To test the newly derived velocity model, we extract 66 well-constrained hypocenters of our catalog (errH, errV < 5.0 km) that occurred in areas known for quarry activity. Since our main scope is passive monitoring of seismotectonic features, we did not go into detail with analyzing the

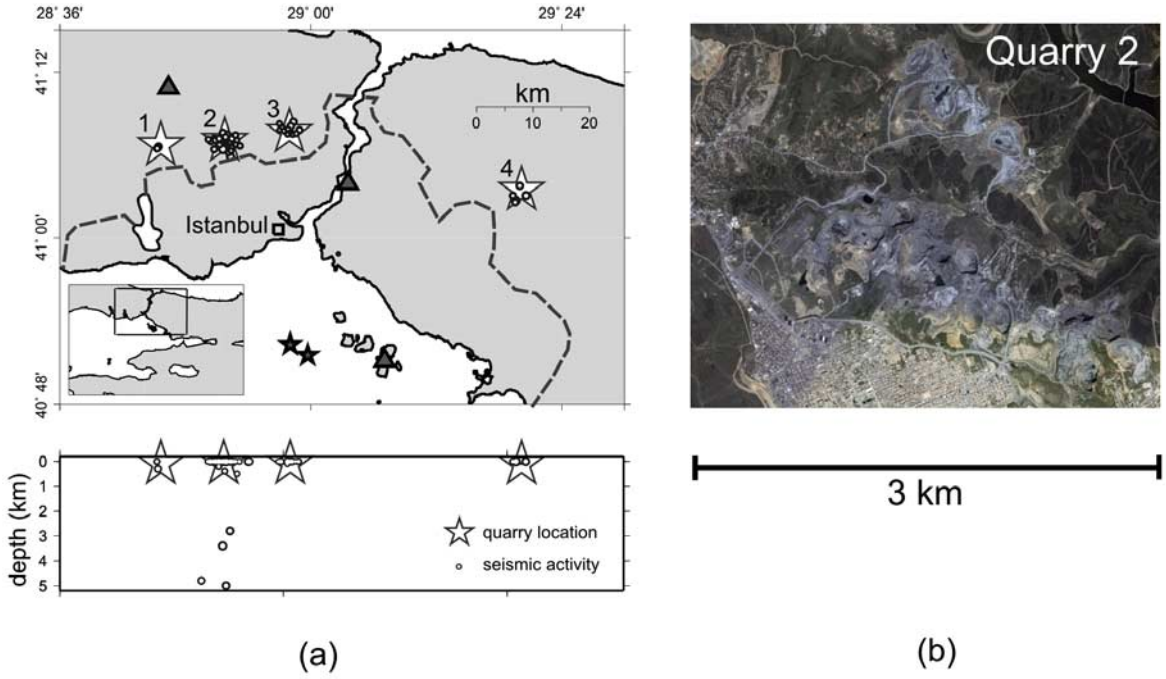


**Figure 7.** (a) Location results compared with quarry locations (stars). The structure of the quarry blasts suggests that a second reason for the scattered map view of blasting events is probably the source aperture, beside the location uncertainty. Dashed line shows the boundary of populated part of Istanbul. (b) Quarry locations confirmed by satellite images.

characteristics of quarry blast waveforms. However, we used some of the basic observations to confirm whether the land clusters associated with quarry blasts. The depth range of the clusters gives first-order information to resolve this issue. We observed that the majority of offshore earthquakes occur below 5.0 km depths, which is approximately the upper boundary of seismogenic zone for the surrounding region. Therefore, we use the clusters with very shallow event depths to verify the location of quarry blasts. Event clusters with shallow depths locate typical quarry structures in the satellite images (Figure 7b). Origin times provide another constrain to discriminate the quarry blasts. We checked the origin times and see that events classified as blasting events occur only within the work hours (0800–1700 LT). This clearly indicates the type of origin. These events are concentrated in two areas NE and NW of Istanbul, respectively (see Figure 7). Initial depth for the quarry blast events is set to 0.0 km but was not fixed during the inversion. We were able to locate these events within 5.0 km distance to the center of quarries. The source aperture of quarries, which is up to 3.0 km, may have a major role on scattered view of events, beside the quality of location results. This test shows that the optimized 1-D velocity model allows us to obtain reliable epicenters and realistic error estimates for the north of the Istanbul region.

[19] We combined PIRES, temporary OBS, and KOERI seismic networks for different time spans to get the highest resolution in hypocenter map of Çınarcık Basin. For the time gap between OBS and PIRES campaigns, we relocate KOERI event database to completely cover the time period of November 2005 to December 2007. Comparing our hypocenter catalog to that of KOERI for the analyzed time period the magnitude of completeness in the Çınarcık Basin was lowered from Mc = 2.6 to Mc = 2.0 (Figure 8). PIRES recordings for the time period 4 October 2006 to 31 December 2007 and 60 days of data from the OBS campaign allow us to locate a total number of 239 earthquakes in the Çınarcık Basin (416 seismic events in eastern Marmara region). For further analysis we restrict the catalog to 182 events surrounding the main branch of NAFZ in the Çınarcık Basin that have an average uncertainty of 2.1 and 2.6 km in horizontal and vertical directions, respectively. These hypocenters are further analyzed in the following for a better identification of the seismic patterns in the Çınarcık Basin. Specifications of the well-constrained hypocenters in the Çınarcık Basin are summarized in Figure 6.

## 5. Fault Plane Solutions

[20] Despite the importance to resolve the present deformation pattern in the eastern Sea of Marmara only few faulting mechanisms were presented in the past and most of them reflect aftershock activity of the 1999 İzmit event rather than background seismicity [*Örgülü and Aktar*, 2001; *Karabulut et al.*, 2002; *Pinar et al.*, 2003; *Sato et al.*, 2004; *Bohnhoff et al.*, 2006]. Resolving focal mechanisms of microearthquakes detected by a sparse seismic network with large azimuthal gaps is not a routine task. For the larger events of our hypocenter catalog that were seen also by most of the mainland stations we determined individual focal mechanisms. In addition, composite fault plane solutions are determined for subclusters of highly similar events within a radius of 5.0 km. We first analyze waveform similarity of closely located events using the cross-correla-

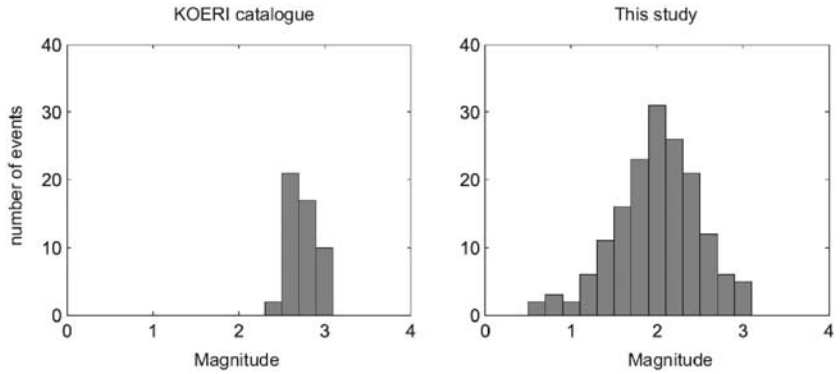


**Figure 8.** Magnitude distribution in Çınarcık Basin from this study compared to the KOERI catalog depicting the decrease in event detection threshold for the same time span between November 2005 and December 2007.

tion technique. The assumption is that we confirm proximity of the events as well as similarity of the mechanisms if the cross-correlation coefficient exceeds 0.6 at a minimum of four stations. Iterating all events as a master to all others we search whether subgroups representing different mechanism exist within the same cluster. If so we treat them individually to derive individual solutions. Figure 4c shows a subgroup of similar events observed at one PIRES subarray. First motion polarities are analyzed to determine the focal mechanisms using the grid search algorithm FOCMEC based on a double-couple assumption [*Snoke*, 2003]. PIRES subarrays are considered to be single stations in this analysis. Confidence range of focal mechanisms is quantified by standard deviation of all acceptable solutions. We determine a total of 18 well-constrained fault plane solutions based on polarity information at a minimum number of 12 stations (Figure 9c and Table 1). We observe a dominant strike-slip mechanism along the northern slope of the Çınarcık Basin where one of the possible fault planes coincides with the local fault strike (N120°E). Toward the western end of the Çınarcık Basin where the NAFZ bends toward the west we observe a substantial thrust component on either NE-SW or NW-SE trending fault planes.

## 6. Discussion

[21] The spatial distribution of the hypocenters obtained from the OBS network and the PIRES array allows to image the currently active fault elements and dominant types of faulting within the eastern Sea of Marmara for the first time. Following the 1999 İzmit earthquake a number of field campaigns were carried out within this part of the NAFZ. Two-dimensional multichannel seismic reflection profiles and high-resolution bathymetry indicate a complex fault network active at the transition between the western end of the İzmit earthquake rupture and the assumed seismic gap south of Istanbul. However, the seismotectonics of the Sea of Marmara are still controversial.

[22] At the easternmost part of the Sea of Marmara just south of the Prince Islands the NAFZ branches in two prominent offshore fault segments [*Armijo et al.*, 2002] that bound the Çınarcık Basin on the NE and SE where most of the 18–20 mm/a GPS-derived dextral displacement is believed to be occurring at present [*Flérit et al.*, 2004]. *Le Pichon et al.* [2001] and *İmren et al.* [2001] proposed that the northern segment is a master strike-slip fault extending throughout the Sea of Marmara. In contrast, on the basis of the same data set, *Armijo et al.* [2002] suggested more active extension with the Çınarcık Basin surrounded by composite normal and strike-slip faults. Multichannel seismic profiles image the main segments of the NAFZ at shallow depth (<5 km) as extending along the northern and southern boundary of the Çınarcık Basin (ÇB) [*Carton et al.*, 2007] forming the downdip extensions of the NAFZ fault traces observed at the sea bottom from high-resolution bathymetric imaging [e.g., *Armijo et al.*, 2005]. Within the southern part of the Çınarcık Basin the structural model is complicated by a number of NW-SE oriented fault segments covering a ~10 km wide zone across the basin. (Çınarcık extensional field [*Le Pichon et al.*, 2001]). Previous locations of local seismicity in Çınarcık Basin (e.g., KOERI catalog) imply a complicated structure rather than one single (strike-slip or normal) fault cutting through the basin (Figure 2a).

[23] In contrast, the microearthquakes observed in this study define a pair of distinct lineations of activity along the northern strand of the NAFZ extending offshore the Prince Islands. The earthquakes primarily align along NW-SE striking features that reflect local activity along the main northern branch of the fault (Figure 9b). Note that the trend of these active patches also aligns with the right-lateral focal mechanisms of the events. The fact that we observe a substantial amount of microseismicity along the east of the "seismic gap" may indicate that the NAFZ is not entirely locked here. However, although the microseismicity indicated ~110°N NW-SE trending subparallel fault segments, it is also possible that the hypocenters are located on structures in the host rock surrounding the fault. Longer monitoring period as well as better station coverage is needed to resolve this issue.

[24] We select three transects (A, B, and C) along the northern slope of the Çınarcık Basin striking NE-SW and perpendicular to the local fault trend (see Figures 9a and 9b). The widths of the transects are 35.0, 16.0, and 16.0 km We then plot all events along the three transects in a depth section for both the KOERI (Figure 9d) and our data set (Figure 9e).

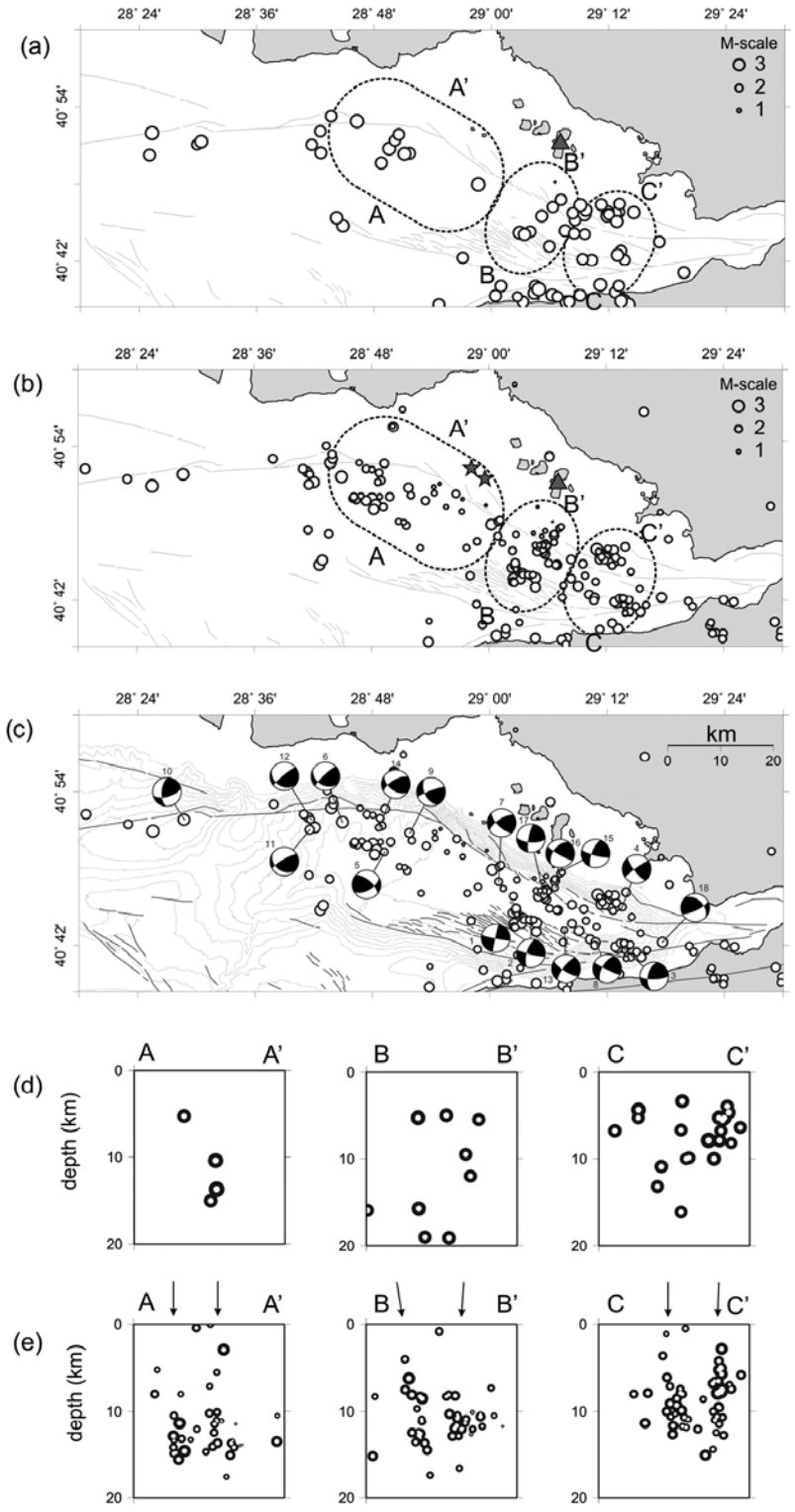


**Figure 9.** (a and d) Hypocenter catalogs obtained from KOERI and (b and e) from this study for the same time span to show the contribution of our experiment to the resolution of hypocenter map of ÇB between November 2005 and December 2007. Hypocenter map obtained in this study allows us to better resolve individual activity patches. Orientation of the hypocenters along the Çınarcık Basin confirms NW-SE strike of focal mechanisms. (c) Composite fault plane solutions derived from first-motion approach.

**Table 1.** Composite Fault Plane Solutions

| Event | Location of Master Event | | | Focal Mechanism (deg) | | | Standard Deviation (deg) | | | Number of Data | Number of Misfits |
|---|---|---|---|---|---|---|---|---|---|---|---|
| | Latitude (°E) | Longitude (°N) | Depth (km) | Strike | Dip | Rake | Strike | Dip | Rake | | |
| 1 | 40.735 | 29.057 | 10.2 | 192 | 88 | 5 | 7 | 3 | 3 | 33 | 4 |
| 2 | 40.734 | 29.058 | 10.4 | 196 | 66 | 7 | 4 | 2 | 4 | 31 | 2 |
| 3 | 40.699 | 29.227 | 5.5 | 191 | 54 | 21 | 7 | 3 | 4 | 44 | 3 |
| 4 | 40.761 | 29.195 | 7.8 | 234 | 84 | 15 | 9 | 4 | 6 | 41 | 5 |
| 5 | 40.821 | 28.791 | 9.9 | 60 | 57 | 33 | 8 | 14 | 8 | 25 | 4 |
| 6 | 40.869 | 28.741 | 3.7 | 226 | 80 | 55 | 5 | 5 | 7 | 37 | 4 |
| 7 | 40.812 | 28.989 | 13.8 | 236 | 67 | 26 | 8 | 11 | 5 | 22 | 3 |
| 8 | 40.704 | 29.174 | 7.4 | 209 | 61 | 5 | 15 | 10 | 5 | 21 | 6 |
| 9 | 40.846 | 28.856 | 11.4 | 249 | 83 | 38 | 3 | 3 | 4 | 33 | 5 |
| 10 | 40.859 | 28.467 | 6.5 | 184 | 60 | 33 | 12 | 13 | 9 | 13 | 2 |
| 11 | 40.852 | 28.69 | 7.4 | 239 | 78 | 60 | 5 | 9 | 18 | 27 | 4 |
| 12 | 40.866 | 28.68 | 5.4 | 230 | 82 | 62 | 9 | 6 | 8 | 31 | 4 |
| 13 | 40.747 | 29.114 | 8.2 | 217 | 74 | 16 | 10 | 25 | 7 | 19 | 5 |
| 14 | 40.854 | 28.805 | 12.5 | 239 | 65 | 44 | 6 | 4 | 3 | 38 | 3 |
| 15 | 40.788 | 29.123 | 10.4 | 200 | 69 | 12 | 11 | 13 | 10 | 27 | 4 |
| 16 | 40.777 | 29.1 | 9.5 | 217 | 49 | 11 | 5 | 3 | 2 | 32 | 2 |
| 17 | 40.764 | 29.092 | 8.7 | 190 | 77 | 25 | 6 | 4 | 3 | 39 | 3 |
| 18 | 40.707 | 29.292 | 13.8 | 64 | 74 | 49 | 3 | 4 | 5 | 23 | 2 |

[25] Below the Çınarcık Basin seismic activity reveals NW-SE alignment of hypocenters in accordance with the trend of the NAFZ. The quality of hypocenter determination and the detection threshold of seismic events are very similar along the entire Çınarcık Basin. The eastern transects (B-B′, C-C′) show that the seismic activity is more pronounced in the east of 29°E. The difference in seismic activity might be related to a variation in local stresses along the fault toward the western termination of the 1999 İzmit rupture [*Karabulut et al.*, 2002; *Özalaybey et al.*, 2002]. The hypocenter distribution indicates two downdipping structures. The first group, at the entire northern boundary of the Çınarcık Basin, is steeply dipping to the SW. We interpret this as the major branch of the NAFZ in the Sea of Marmara along the northern slope of the Çınarcık Basin.. The second group defines two subclusters oriented parallel to the first group on average. Surface projection of this two sub clusters coincide with the surface gas emissions observed by *Geli et al.* [2008]. This might represent the merging of both fault branches to a single master fault representing the NAFZ below the seismogenic layer of the crust beneath the Çınarcık Basin.

[26] *Sato et al.* [2004] operated two local OBS networks for a time period of 30 days each. They observed two seismicity clusters distributed along the eastern and western part of Çınarcık Basin. The one observed in the west was interpreted to represent a steeply southward dipping "Main Marmara Fault" beneath the northern slope of Çınarcık Basin. However, it might partly suggest a continuation of the southern group of activity described in this study. *Carton et al.* [2007] imaged single fault zone throughout both clusters based on high-resolution seismic data. The cross sections confirm the downdip continuation of the microseismic events at depth while the surface projection corresponds to the NW-SE striking boundary faults surrounding the Çınarcık Basin. Carton et al. also provide a seismic profile covering part of the section B-B′ imaging the shallower part of the Basin. Plotting the seismic section obtained from high-resolution multichannel seismic together with the hypocentral distribution as determined in this study shows a clear correlation between the downdip extension of the major fault branches seen in the reflection data with the hypocenters below the eastern Sea of Marmara (Figure 11). In cross section the hypocenter distribution defines the downward extension of the major faults bounding the Çınarcık Basin. The upper parts of these faults are clearly shown in the shallow seismic images. The steep dip of these faults appears to be relatively constant down to a depth of >15 km. Only at a depth >17 km the faults seem to merge and the NAFZ may act as one master fault.

[27] At the easternmost part of the Çınarcık Basin two well-developed activity clusters occurred near the coastlines of Tuzla in the north and Armutlu Peninsula in the south (profile C-C′). The hypocenters are aligned forming two parallel elongate clusters following the northern escarpment of Çınarcık Basin. Both clusters were activated after the 1999 İzmit earthquake with pronounced aftershock activity that was also revealed during the OBS campaign in 2000 [*Sato et al.*, 2004]. In cross section the hypocenters indicate an almost vertical fault segment in agreement with relocated aftershocks of the İzmit earthquake [*Bulut and Aktar*, 2007]. South of the Çınarcık Basin a series of individual hypocenter clusters delineate a NW-SE to E-W trending fault segments (Figure 9b) that are steeply dipping toward the north.

[28] Fault plane solutions for the eastern Sea of Marmara as presented above show a predominant dextral strike-slip regime along the northern strand of the NAFZ bounding the Çınarcık Basin. Most likely the NW-SE striking nodal planes of the focal mechanisms represent the fault plane thus correlating well with the local fault trend. The deformation pattern changes toward the west at the bending point of the NAFZ where a substantial thrust component is present in the mechanisms. Kinematically, this makes sense within this compressional bend, and suggests an added component of fault normal compression along this E-W trending segment as opposed to the pure strike slip motion along the northern slope of the Çınarcık Basin. Strike slip motion along the northern slope of the Çınarcık Basin is also suggested by fault plane solutions of İzmit aftershocks [*Örgülü and Aktar*, 2001; *Karabulut et al.*, 2002; *Pinar et al.*, 2003; *Bohnhoff et al.*, 2006] (Figure 10).

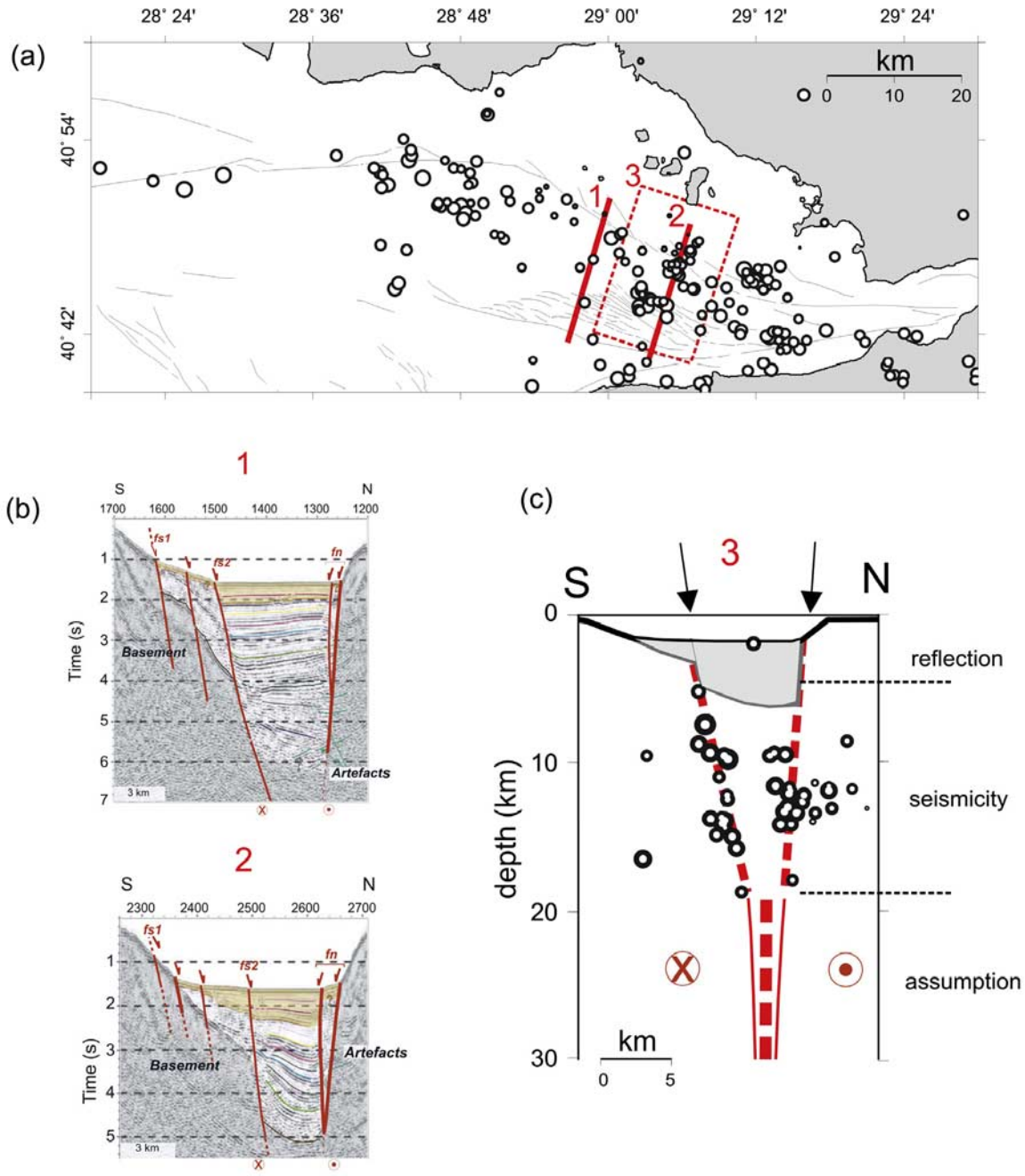


**Figure 10.** (a) Map view of the sectional view of seismicity with shallow seismic profiles. (b) Seismic profiles 1 and 2 (locations indicated in Figure 10a) and (c) seismic profile 3 (location indicated in Figure 10a) showing the boundary of the hypocentral area that we include in sectional view of seismicity. Hypocenter distribution is in agreement with the downdip extent of the shallow structures imaged by *Carton et al.* [2007] within the seismogenic zone. This suggests that both fault segments merge below ~17 km depth (see dashed lines in Figure 10c).

[29] In a transform zone, the direction of the maximum principal stress can vary within a large margin with regard to the fault strike [*McKenzie and Parker*, 1967]. The actual angle between both directions may be related to either the physical nature of the fault zone (weak versus strong) or the stage of the fault in its earthquake cycle (interseismic, preseismic, coseismic or postseismic period). With an increasing portion of the extension, the maximum principal stress would then be rotated toward vertical. The region throughout NW Turkey and in particular the Sea of Marmara is located in a combined strike-slip and normal faulting setting. Normal faulting in the southern Sea of Marmara region is a well-known feature [e.g., *Parke et al.*, 2002] as can be observed from fault plane solutions of several large events (see also Figure 1b). In 1963, a M6.3 earthquake occurred in the eastern Sea of Marmara that was located in the south of the Çınarcık Basin [*Bulut and Aktar*, 2007]. Its fault plane solution indicates N-S extensional

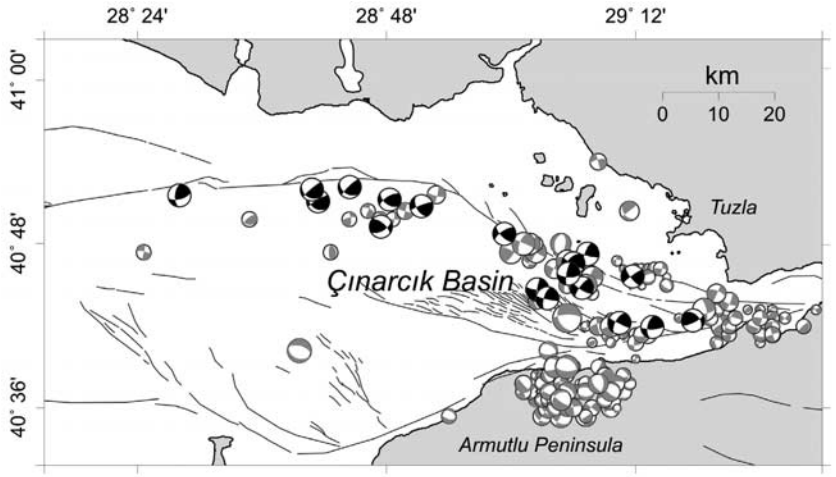


**Figure 11.** Composite fault plane solutions obtained in this study (black beach ball) indicates a dominant NW-SE oriented strike-slip regime along the northern Çınarcık Basin. This is confirmed by the solutions from the analysis of 1999 İzmit aftershocks (gray beach ball) compiled from *Örgülü and Aktar* [2001], *Karabulut et al.* [2002], and *Pinar et al.* [2003].

normal faulting mechanism [*Taymaz et al.*, 1991]. In addition, a large portion of the 1999 İzmit aftershocks of this region were normal faulting events (see Figure 10) representing a more vertical orientation of the P axis. On the other hand, the bending of the NAFZ in the Çınarcık Basin from E-W toward a NW-SE orientation indicated a subhorizontal P axis rotated ~20° clockwise with respect to the regional trend. Slight variation in the strike of local activity patches indicates internal deformations within the boundaries of this ~5 km wide activity zone in which direction of maximum shear stress might differ from that further to the east. The state of the stress field along the Çınarcık Basin is still not well known and needs to be investigated using a larger data set before our observation can be related to local variations in the stress field orientation. Furthermore, a refined knowledge on the stress field of the region might resolve whether this part of the NAFZ reflects a weak or a strong fault. Nonetheless, assuming a weak transform fault in the north and observing a majority of normal faulting activity in the south, we can state that the asymmetry of the Çınarcık Basin can be explained by a transform-normal extension as a possible alternative to pull-apart models [*Ben-Avraham and Zoback*, 1992].

[30] One principal observation from the analysis of faulting mechanisms along the eastern "seismic gap" suggests that currently normal faulting does not seem to play a major role below the eastern Sea of Marmara. At least locally this suggests a transpressive regime rather than normal faulting. However, a thrust component seen near Istanbul represent the potential for uplift during a large event, with the potential to generate a substantial tsunami as has been observed in historic times [*Yalciner et al.*, 2002].

## 7. Conclusion

[31] We quantified applicability of the cross-correlation method for azimuth estimations comparing azimuth of well constrained hypocenters with cross-correlation–derived azimuth observations. Covariance-based error estimates provide sufficient reliability for the confidence range of azimuths. Our investigations show that the number of station pairs is the most important criteria to better constrain the azimuth observations.

[32] We optimized a 1-D velocity model for the eastern Sea of Marmara region and depicted its benefit in terms of uncertainty and misfit of the absolute locations. Blast events confirm the reliability of confidence range of the hypocenters determined on the basis of optimized 1-D velocity model.

[33] We monitor the present-day microseismic activity in Çınarcık Basin at a magnitude of completeness 2.0 using the PIRES seismic array. The distribution of hypocenters allows us to provide an indication of a relatively complex network of faults beneath Çınarcık Basin rather than a single fault zone cutting through. Our results imply a wedge-shaped geometry of the Çınarcık Basin.

[34] Fault plane solutions confirm the analysis of 1999 İzmit aftershocks, and therefore allow us to conclude that a right-lateral strike-slip regime still dominates the Çınarcık Basin region. This might suggest that an upcoming major earthquake in the eastern Sea of Marmara region is likely to be a strike slip event.

[35] **Acknowledgments.** We thank Mark Zoback, an anonymous reviewer, and the Associate Editor for their constructive comments that helped to improve the manuscript. We are grateful to Dean Childs, Michael Naumann, Yaman Ozakın, and Ethem Gorgun for the installation and maintenance of the PIRES array and to Geophysical Instrument Pool of GFZ Potsdam for supplying us with stations for the initial recording period of PIRES. GeoPro Ltd., Germany, has operated the temporary OBS campaign. We thank Dogan Kalafat and KOERI National Earthquake Monitoring Center for sharing digital recordings. GMT (Generic Mapping Tools) code has been used to plot some of the figures [*Wessel and Smith*, 1995].

## References

Aktar, M., S. Özalaybey, M. Ergin, H. Karabulut, M.-P. Bouin, C. Tapırdamaz, F. Biçmen, A. Yörük, and M. Bouchon (2004), Fault zone heterogeneity and variations of seismicity parameters across 1999 İzmit-Düzce earthquake sequence, *Tectonophysics*, *391*, 325–334, doi:10.1016/j.tecto.2004.07.020.

Ambraseys, N. N. (1970), Some characteristic features of the North Anatolian Fault Zone into the north Aegean, *Tectonophysics*, *9*, 143–165, doi:10.1016/0040-1951(70)90014-4.

Armijo, R., B. Meyer, S. Navarro, G. King, and A. Barka (2002), Asymmetric slip partitioning in the Sea of Marmara pull-apart: A clue to propagation processes of the North Anatolian Fault, *Terra Nova*, *14*, 80–86, doi:10.1046/j.1365-3121.2002.00397.x.

Armijo, R., et al. (2005), Submarine fault scarps in the Sea of Marmara pull-apart (North Anatolian Fault): Implications for seismic hazard in Istanbul, *Geochem. Geophys. Geosyst.*, *6*, Q06009, doi:10.1029/2004GC000896.

Barış, S., A. Ito, S. B. Üçer, Y. Honkura, N. Kafadar, R. Pektaş, T. Komut, and A. M. Işıkara (2002), Microearthquake activities before the İzmit earthquake in the eastern Marmara region, Turkey (Jan.1, 1993–Aug. 17, 1999), *Bull. Seismol. Soc. Am.*, *92*, 394–405, doi:10.1785/0120000826.

Barka, A. (1992), The North Anatolian Fault, *Ann. Tectonicae*, *6*, 164–195.

Barka, A. (1999), The 17 August İzmit earthquake, *Science*, *285*, 1858–1859, doi:10.1126/science.285.5435.1858.

Barka, A., et al. (2002), The surface rupture and slip distribution of the 17 August 1999 İzmit earthquake (M 7.4), North Anatolian Fault, *Bull. Seismol. Soc. Am.*, *92*, 43–60, doi:10.1785/0120000841.

Ben-Avraham, Z., and M. D. Zoback (1992), Transform-normal extension and asymmetric basins: An alternative to pull-apart models, *Geology*, *20*(5), 423–426, doi:10.1130/0091-7613(1992)020<0423:TNEAAB>2.3.CO;2.

Bohnhoff, M., H. Grosser, and G. Dresen (2006), Strain partitioning and stress rotation at the North Anatolian fault zone from aftershock focal mechanisms of the 1999 İzmit Mw = 7.4 earthquake, *Geophys. J. Int.*, *166*, 373–385, doi:10.1111/j.1365-246X.2006.03027.x.

Bokelmann, G. H. R. (1995), Azimuth and slowness deviations from the GERESS regional array, *Bull. Seismol. Soc. Am.*, *85*, 1456–1463.

Bouchon, M., M. N. Töksöz, H. Karabulut, M.-P. Bouin, M. Dietrich, M. Aktar, and M. Edie (2002), Space and time evolution of rupture and faulting during the 1999 İzmit (Turkey) earthquake, *Bull. Seismol. Soc. Am.*, *92*, 256–266, doi:10.1785/0120000845.

Bulut, F., and M. Aktar (2007), Accurate relocation of İzmit earthquake (Mw = 7.4, 1999) aftershocks in Çınarcık Basin using double difference method, *Geophys. Res. Lett.*, *34*, L10307, doi:10.1029/2007GL029611.

Cansi, Y., J. L. Plantet, and B. Massinon (1993), Earthquake location applied to a mini-array: K-spectrum versus correlation method, *Geophys. Res. Lett.*, *20*, 1819–1822, doi:10.1029/93GL01397.

Carton, H., et al. (2007), Seismic imaging of the three-dimensional architecture of the Çınarcık Basin along the North Anatolian Fault, *J. Geophys. Res.*, *112*, B06101, doi:10.1029/2006JB004548.

Efron, B. (1982), The jacknife, the bootstrap, and other resampling plans, report, 92 pp., Soc. for Ind. and Appl. Math., Philadelphia, Pa.

Ergin, M., M. Aktar, F. Biçmen, A. Yörük, N. Yalçın, and S. Kuleli (1997), İzmit körfezi mikrodeprem çalışması, paper presented at Aktif Tektonik Araştırma Grubu 1. Toplantısı, Aktif Tektonik Araştırma Grubu, Istanbul, Turkey, 8–9 Dec.

Flérit, F., R. Armijo, G. King, and B. Meyer (2004), The mechanical interaction between the propagating North Anatolian Fault and the back-arc extension in the Aegean, *Earth Planet. Sci. Lett.*, *224*, 347–362, doi:10.1016/j.epsl.2004.05.028.

Frankel, A., S. Hough, P. Friberg, and R. Busby (1991), Observations of Loma Prieta aftershocks from a dense array in Sunnyvale, California, *Bull. Seismol. Soc. Am.*, *5*, 1900–1922.

Geli, L., et al. (2008), Gas emissions and active tectonics within the submerged section of the North Anatolian Fault zone in the Sea of Marmara, *Earth Planet. Sci. Lett.*, *274*, 34–39, doi:10.1016/j.epsl.2008.06.047.

Hubert-Ferrari, A., A. Barka, E. Jacques, S. S. Nalbant, B. Meyer, R. Armijo, P. Traponnier, and G. C. P. King (2000), Seismic hazard in the Marmara Sea following the 17 August 1999 İzmit earthquake, *Nature*, *404*, 269–273, doi:10.1038/35005054.

İmren, C., X. Le Pichon, C. Rangin, E. Demirbag, B. Ecevitoglu, and N. Gorur (2001), The North Anatolian Fault within the Sea of Marmara: A new interpretation based on multichannel seismic and multi-beam bathymetry data, *Earth Planet. Sci. Lett.*, *186*, 143–158, doi:10.1016/S0012-821X(01)00241-2.

Jurkevics, A. (1988), Polarization analysis of three-component array data, *Bull. Seismol. Soc. Am.*, *78*, 1725–1743.

Karabulut, H., M.-P. Bouin, M. Bouchon, M. Dietrich, C. Cornou, and M. Aktar (2002), The seismicity in the eastern Marmara Sea after the 17 August 1999 İzmit earthquake, *Bull. Seismol. Soc. Am.*, *92*, 387–393, doi:10.1785/0120000820.

Kissling, E., W. L. Ellsworth, D. Eberhart-Philipps, and U. Kradolfer (1994), Initial reference models in local earthquake tomography, *J. Geophys. Res.*, *99*, 19,635–19,646, doi:10.1029/93JB03138.

LePichon, X., T. Taymaz, and C. Sengör (1999), The Marmara fault and the future Istanbul earthquake, in *ITU-IAHS International Conference on the Kocaele Earthquake 17 August 1999*, edited by M. Karaca and D. N. Ural, pp. 41–54, Istanbul Tech. Univ., Istanbul.

LePichon, X., et al. (2001), The active Main Marmara Fault, *Earth Planet. Sci. Lett.*, *192*, 595,616.

Lienert, B. R., and J. Havskov (1995), HYPOCENTER 3.2—A computer program for locating earthquakes locally, regionally and globally, *Seismol. Res. Lett.*, *66*, 26–36.

McClusky, S., et al. (2000), Global Positioning System constraints on plate kinematics and dynamics in the eastern Mediterranean and Caucasus, *J. Geophys. Res.*, *105*, 5695–5719.

McKenzie, D. P., and R. L. Parker (1967), The North Pacific: An example of tectonics on a Sphere, *Nature*, *216*, 1276–1280, doi:10.1038/2161276a0.

Menke, W. (1984), *Geophysical Data Analysis: Discrete Inverse Theory*, Academic, New York.

Oglesby, D. D., P. M. Mai, K. Atakan, and S. Pucci (2008), Dynamic models of earthquakes on the North Anatolian fault zone under the Sea of Marmara: Effect of hypocenter location, *Geophys. Res. Lett.*, *35*, L18302, doi:10.1029/2008GL035037.

Örgülü, G., and M. Aktar (2001), Regional moment tensor inversion for strong aftershocks of the August 17, İzmit earthquake (Mw = 7.4), *Geophys. Res. Lett.*, *28*, 371–374, doi:10.1029/2000GL011991.

Oye, V., and M. Roth (2003), Automatic seismic event location for hydrocarbon reservoirs, *Comput. Geosci.*, *29*, 851–863, doi:10.1016/S0098-3004(03)00088-8.

Özalaybey, S., M. Ergin, M. Aktar, C. Tapirdamaz, F. Bicman, and A. Yörük (2002), The 1999 İzmit earthquake sequence in Turkey: Seismological and tectonic aspects, *Bull. Seismol. Soc. Am.*, *92*, 376–386, doi:10.1785/0120000838.

Parke, J. R., R. S. White, D. McKenzie, T. A. Minshull, J. M. Bull, I. Kuşçu, N. Görür, and C. Şengör (2002), Interaction between faulting and sedimentation in the Sea of Marmara, western Turkey, *J. Geophys. Res.*, *107*(B11), 2286, doi:10.1029/2001JB000450.

Parsons, T. (2004), Recalculated probability of $M \geq 7$ earthquakes beneath the Sea of Marmara, Turkey, *J. Geophys. Res.*, *109*, B05304, doi:10.1029/2003JB002667.

Parsons, T., S. Toda, R. S. Stein, A. Barka, and J. H. Dieterich (2000), Heightened odds of large earthquakes near Istanbul: An interaction-based probability calculation, *Science*, *288*, 661–664, doi:10.1126/science.288.5466.661.

Pinar, A., Y. Honkura, and K. Kuge (2001), Seismic activity triggered by the 1999 İzmit earthquake and its implications for the assessment of future seismic risk, *Geophys. J. Int.*, *146*, F1–F7, doi:10.1046/j.0956-540x.2001.01476.x.

Pinar, A., K. Kuge, and Y. Honkura (2003), Moment tensor inversion of recent small to moderate sized earthquakes: Implications for seismic hazard and active tectonics beneath the Sea of Marmara, *Geophys. J. Int.*, *153*, 133–145, doi:10.1046/j.1365-246X.2003.01897.x.

Poupinet, G., W. L. Ellsworth, and J. Frechet (1984), Monitoring velocity variations in the crust using earthquake doublets: An application to the Calaveras Fault, California, *J. Geophys. Res.*, *89*, 5719–5731, doi:10.1029/JB089iB07p05719.

Reilinger, R., N. Toksoz, S. McClusky, and A. Barka (2000), 1999 İzmit, Turkey, earthquakes was no surprise, *GSA Today*, *10*(1), 1–6.

Sato, T., J. Kasahara, T. Taymaz, M. Ito, A. Kamimura, T. Hayakawa, and O. Tan (2004), A study of microearthquake seismicity and focal mechanisms within the Sea of Marmara (NW Turkey) using ocean bottom seismometers (OBSs), *Tectonohysics*, *391*, 303–314, doi:10.1016/j.tecto.2004.07.018.

Segall, P., and M. V. Matthews (1988), Displacement calculation from geodetic data and the testing of geophysical deformation models, *J. Geophys. Res.*, *93*, 14,954–14,966, doi:10.1029/JB093iB12p14954.

Şengör, A. M. C., O. Tüysüz, C. İmren, M. Sakınç, E. Eyidoğan, N. Görür, X. Le Pichon, and C. Rangin (2005), The North Anatolian Fault: A new look, *Annu. Rev. Earth Planet. Sci.*, *33*, 37–112, doi:10.1146/annurev.earth.32.101802.120415.

Shearer, P. (1997), Improving local earthquake locations using the L1 norm and waveform cross correlation: Application to the Whittier Narrows, California, aftershock sequence, *J. Geophys. Res.*, *102*, 8269–8283, doi:10.1029/96JB03228.

Snoke, J. A. (2003), FOCMEC: FOcal MEChanism determinations, in *International Handbook of Earthquake and Engineering Seismology*, edited by W. H. K. Lee et al., chap. 85.12, Academic, San Diego, Calif.

Stein, R. S., A. Barka, and J. H. Dieterich (1997), Progressive failure of the North Anatolian Fault since 1939 by earthquake stress triggering, *Geophys. J. Int.*, *128*, 594–604, doi:10.1111/j.1365-246X.1997.tb05321.x.

Taymaz, T., J. Jackson, and D. McKenzie (1991), Active tectonics of the north and central Aegean Sea, *Geophys. J. Int.*, *106*, 433–490, doi:10.1111/j.1365-246X.1991.tb03906.x.

Tibi, R., G. Bock, Y. Xia, M. Baumbach, H. Grosser, C. Milkereit, S. Karakisa, S. Zünbül, R. Kind, and J. Zschau (2001), Rupture processes of the 1999 August 17 İzmit and November 12 Düzce (Turkey) earthquakes, *Geophys. J. Int.*, *144*, F1–F7, doi:10.1046/j.1365-246x.2001.00360.x.

Töksöz, M. N., A. F. Shakal, and A. J. Michael (1979), Space-time migration of earthquakes along the North Anatolian Fault and seismic gaps, *Pure Appl. Geophys.*, *117*, 1258–1270, doi:10.1007/BF00876218.

U.S. Geological Survey (2000), Implications for Earthquake Risk Reduction in the United States from the Kocaeli, Turkey Earthquake of August 17, 1999, *U. S. Geol. Surv. Circ.*, *1193*.

Waldhauser, F., and W. L. Ellsworth (2000), A double-difference earthquake location algorithm: Method and application to the northern Hayward fault, *Bull. Seismol. Soc. Am.*, *90*, 1353–1368, doi:10.1785/0120000006.

Wessel, P., and W. H. F. Smith (1995), New version of the generic mapping tools released, *Eos Trans. AGU*, *76*(33), 329, doi:10.1029/95EO00198.

Wright, T., E. Fielding, and B. Parsons (2001), Triggered slip: Observations of the 17 August 1999 İzmit (Turkey) earthquake using radar interferometry, *Geophys. Res. Lett.*, *28*, 1079–1082, doi:10.1029/2000GL011776.

Yalciner, A. C., B. Alpar, Y. Altinok, I. Özbay, and F. Imamura (2002), Tsunamis in the Sea of Marmara: Historical documents for the past, models for the future, *Mar. Geol.*, *190*, 445–463, doi:10.1016/S0025-3227(02)00358-4.

M. Aktar, Kandilli Observatory and Earthquake Research Institute, Boğaziçi University, 34680, Çengelköy, İstanbul, Turkey. (aktar@boun.edu.tr)

M. Bohnhoff, F. Bulut, and G. Dresen, Helmholtz Centre Potsdam, GFZ German Research Centre for Geosciences, Section 3.2, Geomechanics and Rheology, Telegrafenberg D424, D-14473 Potsdam, Germany. (bohnhoff@gfz-potsdam.de; bulut@gfz-potsdam.de; georg.dresen@gfz-potsdam.de)

W. L. Ellsworth, U.S. Geological Survey, 345 Middlefield Road, MS 977, Menlo Park, CA 94025, USA. (ellsworth@usgs.gov)